Nanoscale

PAPER

View Article Online
View Journal | View Issue

Cite this: *Nanoscale*, 2025, **17**, 9213

High-performance aqueous copper-ion batteries based on iron hexacyanoferrate cathodes for enhanced energy storage†

Jinshu Zhang,[a] Lexian Liu,[a] Yuao Wang,[c] Yantuo Li,[a] Yang Yang,[a] Mingyi Ning,[a] Jianxue Wu,[a] Bingjie Ma[a] and Wei Liu *[a,b]

Received 10th December 2024,
Accepted 1st March 2025

DOI: 10.1039/d4nr05203j

rsc.li/nanoscale

The integration of renewable energy sources, such as solar and wind, requires efficient energy storage systems. Aqueous batteries, with their safety, low cost, and flexibility, have gained attention as promising solutions for energy storage. In this study, we developed an aqueous copper-ion storage device based on an iron hexacyanoferrate (FeHCF) cathode, which offers high capacities of 190 mA h g^{-1} at 1 A g^{-1} and 102 mA h g^{-1} even at 3 A g^{-1}, with a discharge plateau at 0.59 V *vs.* SHE and a low polarization voltage of 0.2 V. *In situ* XRD, Raman, and XPS characterization techniques show that copper-ion insertion induces structural changes in FeHCF, leading to a valence state transition between Fe^{2+} and Fe^{3+}, with a partial conversion of Cu^{2+} to Cu^{+}. To improve the working voltage, we replaced the Cu^{2+}/Cu^{0} anode reaction with the lower potential $Zn/Zn(OH)_4^{2-}$ reaction, achieving an aqueous battery with a voltage range of 1.6–2.5 V. These findings highlight FeHCF-based aqueous batteries' potential for high-performance and safe energy storage.

[a]*School of Physics, Key Laboratory of Quantum Materials and Devices of Ministry of Education, Frontiers Science Center for Mobile Information Communication and Security, Southeast University, Nanjing 211189, China.*
E-mail: 101012931@seu.edu.cn
[b]*Purple Mountain Laboratories, Nanjing 211111, China*
[c]*Key Laboratory of Superlight Materials and Surface Technology of Ministry of Education, College of Materials Science and Chemical Engineering, Harbin Engineering University, Harbin 150001, China*
†Electronic supplementary information (ESI) available. See DOI: **https://doi.org/10.1039/d4nr05203j**

Wei Liu

Dr Wei Liu is a Professor at the School of Physics, Southeast University. He received his Bachelor's and Master's degrees in Materials Physics from Sun Yat-sen University. He obtained his Ph.D in NGS from the Department of Chemistry at the National University of Singapore under the supervision of Prof. Loh Kian Ping. After 4 years as a postdoctoral researcher at the National University of Singapore and RIKEN, Japan, he joined Southeast University in 2021. His research interest focuses on innovative synthesis of functional materials for energy storage.

1. Introduction

The transition to renewable energy sources, such as solar, wind, and tidal power, is essential for reducing fossil fuel consumption and improving environmental sustainability.[1,2] However, integrating these energy sources into the grid effectively requires reliable energy storage systems. Electrochemical energy storage systems have attracted significant attention due to their rapid response, flexibility, and environmental friendliness.[3,4] Although lithium-ion batteries currently dominate the energy storage market, their reliance on organic electrolytes raises safety concerns.[5]

Aqueous batteries have emerged as a safer and more cost-effective alternative, attracting interest for their inherent safety and affordability, and they are considered to contribute to the development of green energy and the achievement of carbon neutrality goals.[6–10] The performance of aqueous batteries is significantly influenced by the choice of electrode materials. Prussian blue analogues (PBAs), also known as metal hexacyanoferrates (MHCFs), are particularly promising due to their ease of synthesis and low cost.[11–13] Initially used in applications such as dyeing and energy conversion, PBAs were first explored as electrode materials by Neff *et al.* in 1978, who demonstrated the reversible electrochemical insertion and extraction of K^+ in $K_2Fe^{2+}Fe^{2+}(CN)_6$. This breakthrough paved the way for the development of PBAs in energy storage applications.[14] The open framework structure of PBAs, combined

with transition metals like Zn, Cu, Ni, and Fe, results in large lattice parameters that facilitate ion diffusion and storage. PBAs are now applied as electrode materials in various ion batteries, including Li^+, Na^+, K^+, Zn^{2+} and Mg^{2+} batteries.[15,16] In particular, in aqueous multivalent ion batteries, PBAs have demonstrated high capacity and stable cycling performance, making them a key focus in the advancement of aqueous batteries.[17–20] Among these, iron hexacyanoferrate (FeHCF) stands out due to its high theoretical capacity, simple synthesis, and abundant elemental resources, positioning it as a promising material for energy storage.[21–23]

When FeHCF is used as a zinc-ion storage material, it exhibits a high capacity of 120 mA h g^{-1} at a current density of 0.01 A g^{-1}, with a discharge potential of 0.34 V *vs.* SHE. The charge–discharge voltage difference is approximately 0.4 V.[24] However, at a low current density of 0.06 A g^{-1}, the capacity significantly drops to only 30 mA h g^{-1}. High-voltage scanning can effectively activate the C-coordinated iron in the FeHCF cathode, resulting in higher reaction potentials and improved capacity.[23] Under these conditions, the material achieves a reaction voltage of 0.74 V *vs.* SHE and a capacity of 76 mA h g^{-1} at a high current of 1 A g^{-1}. However, this improvement comes at the trade-off of a wider charge–discharge voltage range, approximately 2.3 V.

Due to the unique redox properties of copper ions, aqueous copper-ion batteries have the potential to further enhance the energy density of aqueous batteries, and related research has been extensively reported in recent years.[25–27] In this study, we report FeHCF nanocrystals as an effective material for copper-ion storage, offering a working voltage of 0.59 V *vs.* SHE. Within a narrower voltage range of 0.6 V, FeHCF delivers a stable discharge plateau and high capacity, reaching 190 mA h g^{-1} at a current density of 1 A g^{-1}. Furthermore, FeHCF exhibits minimal voltage polarization during copper-ion storage, with a voltage difference of 0.2 V, which helps reduce energy loss during the storage process. The storage mechanism of Cu^{2+} in FeHCF was thoroughly investigated using *in situ* X-ray diffraction (XRD), Raman spectroscopy, X-ray photoelectron spectroscopy (XPS), and other characterization techniques. Finally, by using FeHCF as the cathode and Zn/$Zn(OH)_4^{2-}$ as the anode, we constructed an aqueous battery that operates within a voltage range of 1.6–2.5 V, significantly enhancing its potential for practical applications.

2. Results and discussion

FeHCF nanocrystals were prepared using the well-established coprecipitation method.[23] The structure of FeHCF, as shown in Fig. 1a, exhibits a face-centered cubic structure. The FeC_6 and FeN_6 octahedra are connected by CN triple bonds, forming an open framework structure with large spatial voids, which can serve as a fast ion transport channel or storage site. The resulting FeHCF powder consists of fine, uniform cubic particles with edge lengths of approximately 100–200 nm (Fig. 1b and S1†). The nanoscale size provides a larger specific surface area, directly exposing more active sites, which is beneficial for fully activating the energy storage capability of the electrode material.[28] The XRD diffraction pattern of the obtained sample is shown in Fig. 1c, with diffraction peaks matching the characteristic peaks of face-centered cubic FeHCF (PDF#73-0687). The diffraction peaks at 17.5°, 24.8°, 35.4°, and 39.8°

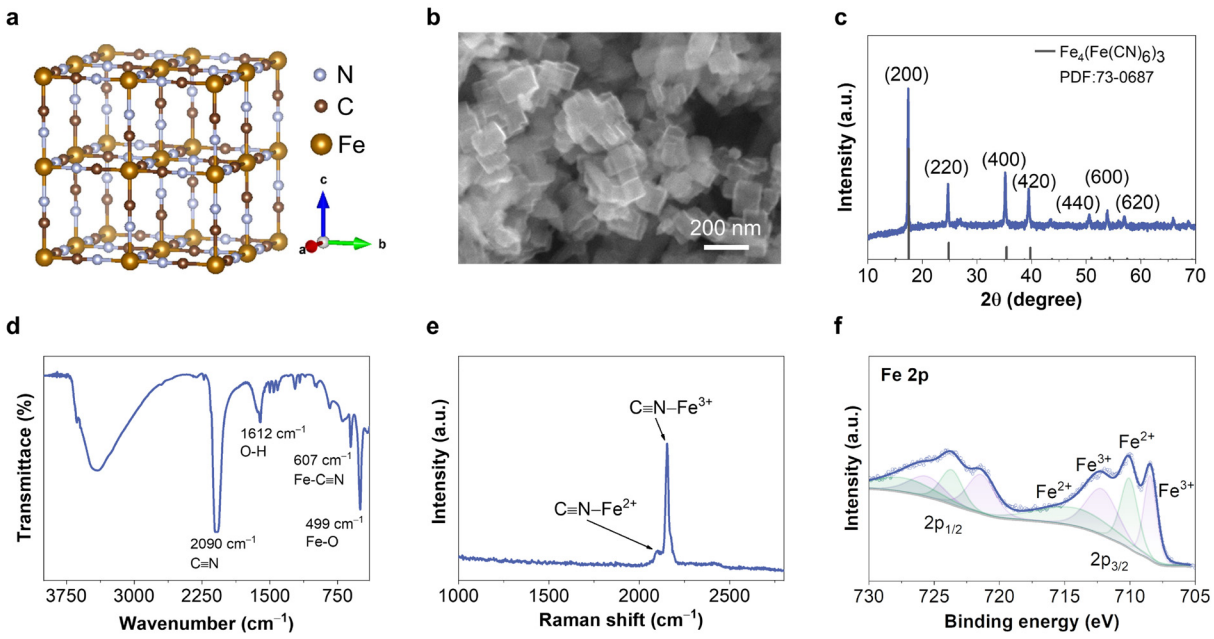

Fig. 1 Morphology, structure and chemical composition of FeHCF. (a) The cubic crystal structure and (b) scanning electron microscopy (SEM) image of FeHCF. (c) XRD patterns, (d) FTIR spectroscopy and (e) Raman spectra of FeHCF. (f) XPS spectra of Fe 2p for FeHCF.

correspond to the (200), (220), (400), and (420) crystal planes, respectively. The chemical structure of FeHCF was characterized by Fourier transform infrared (FTIR) spectroscopy, as shown in Fig. 1d. Peaks at 499 cm^{-1} and 607 cm^{-1} correspond to the out-of-plane bending vibration of Fe–O bonds and the in-plane bending vibration of Fe–C≡N, respectively, while the peak at 2090 cm^{-1} is attributed to the stretching vibration of the C≡N bond.[29] In the Raman spectrum shown in Fig. 1e, the vibration peaks between 2000 and 2200 cm^{-1} represent the characteristic spectra of different valence states of Fe coordinated with cyanide, where the peaks at 2100 cm^{-1} and 2150 cm^{-1} can be assigned to C≡N–Fe^{2+} and C≡N–Fe^{3+}, respectively. In the XPS spectrum shown in Fig. S2,† the presence of C, N, and Fe elements is clearly observed. A detailed XPS spectrum of the Fe 2p orbitals (Fig. 1f) shows fitting peaks at 708.4/721.4 eV and 712.1/725.54 eV corresponding to Fe^{3+} and fitting peaks at 710.0/723.6 eV and 714.1/727.3 eV corresponding to Fe^{2+}.[23] This indicates the coexistence of Fe^{2+} and Fe^{3+} in the synthesized FeHCF powder, consistent with previous reports.[30]

To investigate the copper-ion storage capability of FeHCF, it was used as the working electrode in a coin cell assembled with copper as the counter electrode and 1 M $CuSO_4$ as the electrolyte. Fig. 2a shows the initial cyclic voltammetry (CV) curve of the FeHCF electrode at a scan rate of 0.2 mV s^{-1}. In the first cycle, the first reduction peak appears at 0.39 V *vs.* SHE, which can be attributed to the initial insertion of Cu^{2+} into the FeHCF lattice. In subsequent cycles, a new reduction peak at 0.59 V *vs.* SHE emerges, likely due to the activation of C-coordinated Fe in the FeHCF cathode during higher potential scans.[23] Unlike the zinc-ion storage process, the reduction peak at the lower potential for copper-ion storage does not disappear in the subsequent cycles but gradually stabilizes at around 0.44 V *vs.* SHE. The presence of dual active sites (dual reduction peaks) effectively ensures the copper-ion storage capability of FeHCF. The initial galvanostatic charge/discharge (GCD) curves also reflect this result, as shown in Fig. 2b. During the first discharge cycle, nearly all of the capacity is provided by the discharge plateau at 0.39 V, while in subsequent cycles, the discharge plateau at 0.59 V *vs.* SHE contributes nearly half of the capacity. The decay of the low-potential plateau capacity leads to a decrease in the specific capacity of the FeHCF electrode, but the activation of new active sites alleviates this issue and provides a higher operating potential, which is beneficial for improving the overall energy density of the battery. Furthermore, compared to the storage of other ions such as Zn^{2+}, Al^{3+}, and K^{+}, FeHCF exhibits smaller voltage polarization (~0.2 V) and a narrower charge–discharge window (0.6 V) when storing Cu^{2+}, which better meets the requirements for voltage stability and reduced energy loss in energy storage batteries during use.[23,31–33]

In subsequent long-term cycling, the FeHCF electrode exhibits good stability, as evidenced by the electrochemical impedance spectroscopy (EIS) tests at different cycle numbers (Fig. S3†). In addition, FeHCF is detected in the electrode after 100 cycles, indicating that the active material does not degrade significantly (Fig. S4†). These results contribute to the maintenance of the electrode's electrochemical activity. The copper-ion storage electrochemical performance of the FeHCF electrode in the coin cell was evaluated (Fig. 2c and S5, 6†). As shown in Fig. 2c, at a current density of 1 A g^{-1}, FeHCF (electrochemical tests were conducted under the conditions of FeHCF : super P : PVDF = 7 : 2 : 1 and 1 M $CuSO_4$ electrolyte, unless otherwise specified) provides an initial capacity of 304 mA h g^{-1}; after activation at higher potentials (3 cycles), the capacity is 190 mA h g^{-1}. As mentioned earlier, the initial capacity decay may be due to the reduced activity of the low-

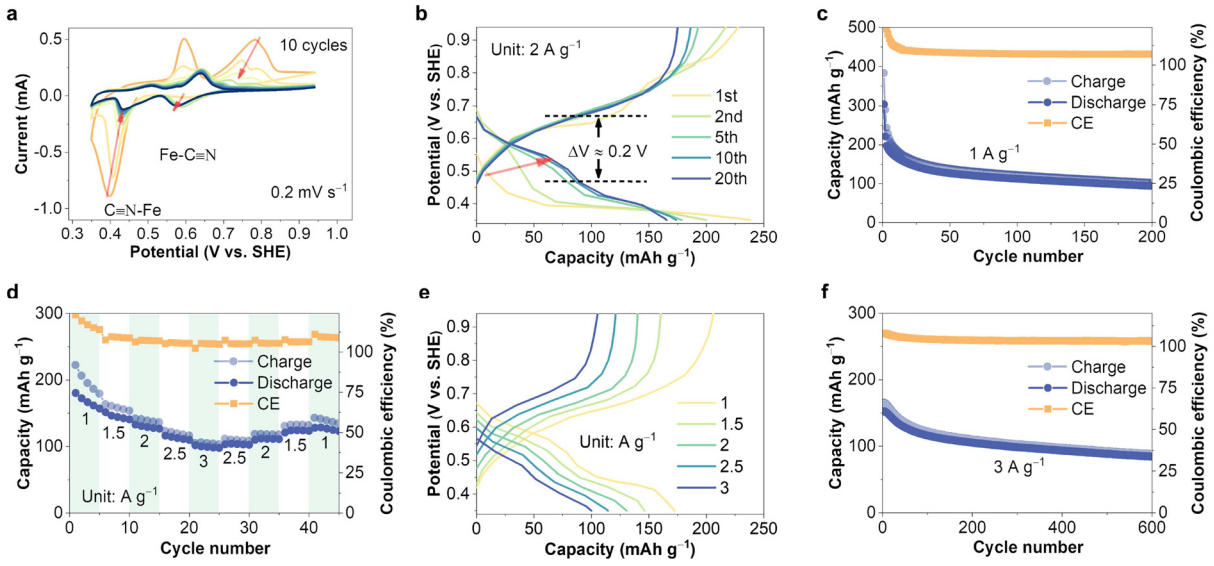

Fig. 2 Electrochemical copper-ion storage performance of FeHCF. (a) *In situ* CV curves recorded at 0.2 mV s^{-1}. (b) Change of the GCD curves of FeHCF. (c) Long-term cycling of the FeHCF electrode (FeHCF : super P : PVDF = 7 : 2 : 1) in 1 M $CuSO_4$ solution at a fixed rate of 1 A g^{-1}. (d) Rate performance and (e) GCD curves of FeHCF at different current densities. (f) Long-term cycling of FeHCF at a fixed rate of 3 A g^{-1}.

potential active sites. At the same time, side reactions such as the partial decomposition of Prussian blue due to water attack can also lead to capacity degradation and the phenomenon where the charging capacity is greater than the discharging capacity.[34,35] Even at higher current densities, the FeHCF electrode retains a capacity of 102 mA h g^{-1} at 3 A g^{-1}, as shown in Fig. 2d. The GCD curves in Fig. 2e show voltage plateaus at approximately 0.44 V *vs.* SHE and 0.59 V *vs.* SHE, with sloping curves at different current densities, indicating that the excellent rate performance is due to the combined maintenance of both battery-type and capacitor-type capacities. At a high current density of 3 A g^{-1}, the FeHCF electrode maintains stable cycling and retains a capacity of 84 mA h g^{-1} after 600 cycles (Fig. 2f). Compared to recent reports on FeHCF-based energy storage devices, these performance metrics are highly competitive, as shown in Fig. S7.†

The reason for the excellent rate performance of the FeHCF electrode was investigated through CV tests at different scan rates, as shown in Fig. 3a. As the scan rate increased from 0.2 to 1 mV s^{-1}, the CV curves showed a systematic change, with only a slight shift in the redox peak positions. This demonstrates the fast redox reaction capability of the FeHCF electrode. The relationship between current (i) and scan rate (v) can be expressed by the following equation:[36]

$$i = av^b \quad (1)$$

where a and b are constant values. Based on the above equation, the log(i) and log(v) values at the oxidation and reduction peaks were linearly fitted. As shown in Fig. 3b, the calculated b-values are b_{peak1} = 0.79, b_{peak2} = 0.74, b_{peak3} = 0.61, and b_{peak4} = 0.57, indicating that the electrochemical reaction of Cu-FeHCF is controlled by both diffusion and capacitive contributions. Furthermore, the following equation can be used to separate the contributions of capacitive and diffusion-controlled capacities:[37]

$$I(V) = k_1 v + k_2 v^{1/2} \quad (2)$$

where k_1 and k_2 can be evaluated by plotting CV current responses at various scan rates. The separation results are

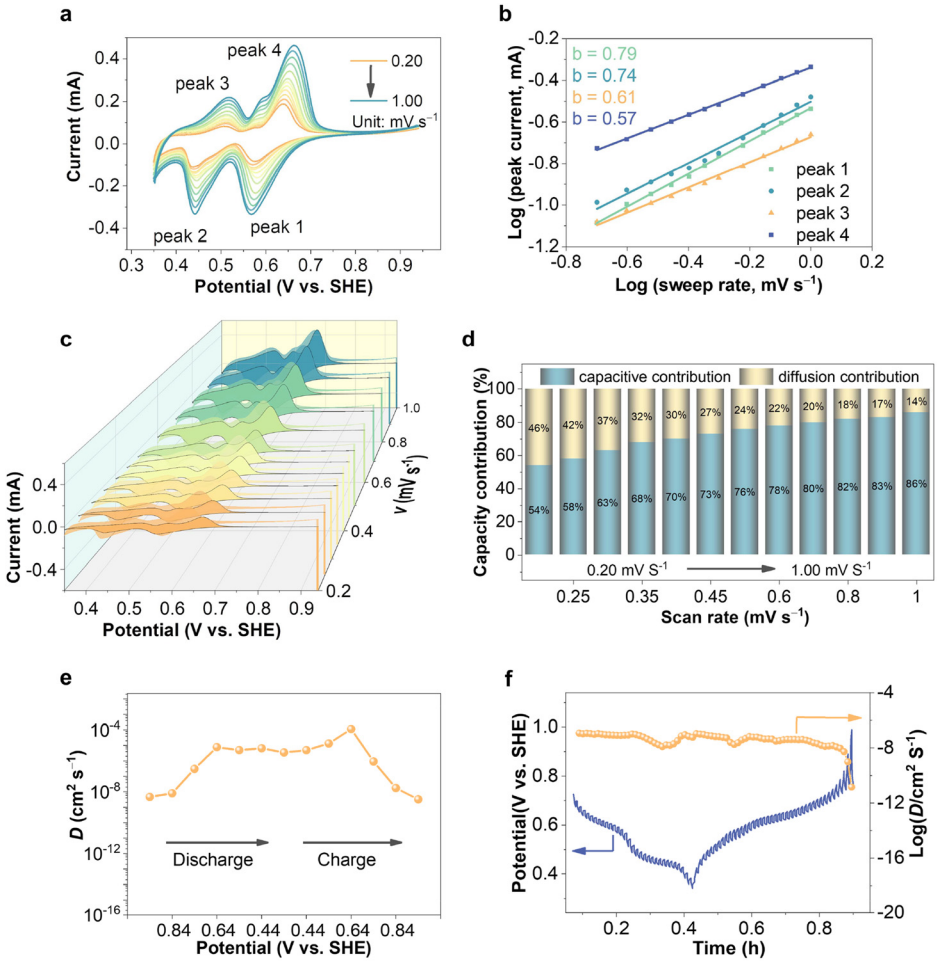

Fig. 3 (a) CV curves of FeHCF at various scan rates. (b) Plots of log(i) *versus* log(v) of FeHCF. (c and d) The pseudocapacitive and diffusion-controlled charge storage contributions at different scan rates of FeHCF. (e) Diffusion coefficient as a function of potential derived from the impedance spectra. (f) Diffusion coefficient of copper-ion of FeHCF measured by the GITT.

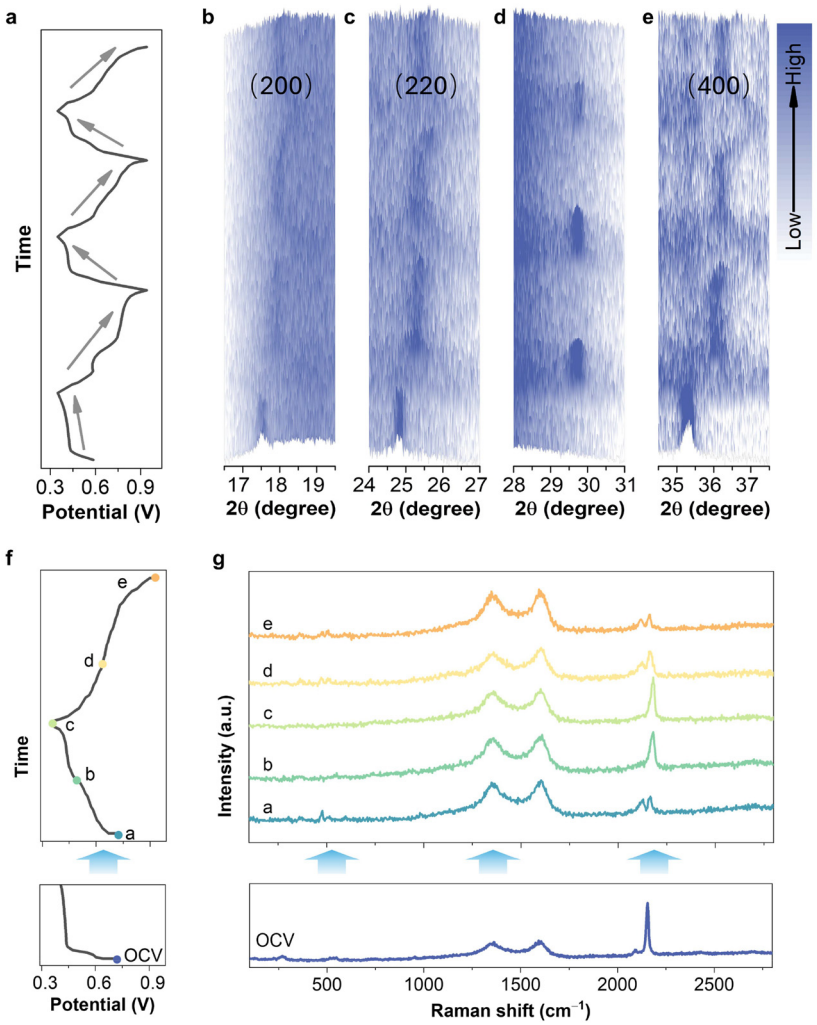

Fig. 4 Evolution of FeHCF during the storage of copper ions. (a) Charge and discharge curves corresponding to *in situ* XRD of the FeHCF electrode. (b–e) The *in situ* XRD curve of FeHCF corresponding to (a). (f) Charge and discharge curves and (g) Raman spectra of FeHCF at the corresponding potentials in (f).

shown in Fig. 3c and d. As the scan rate increases, the contribution of capacitive capacity increases significantly, which may be related to the smaller particle size of FeHCF. During the storage process, the ion diffusion coefficient of Cu^{2+} in the FeHCF electrode can be obtained from EIS tests at different voltage states (Fig. S8†), using the following equation:[38]

$$D = \frac{1}{2}\left[\left(\frac{V_m}{FA\sigma}\right)\left(\frac{dE}{dx}\right)\right]^2 \quad (3)$$

where V_m is the molar volume, F is the Faraday constant, E is the electrode potential, x is the stoichiometry of Cu, and σ is the Warburg factor, which is obtained from the slope of Z' or $-Z''$ *vs.* $\omega^{-1/2}$. The calculation results are shown in Fig. 3e. At different voltage states, the diffusion coefficient of Cu^{2+} in FeHCF remains within the range of 10^{-9} to 10^{-4} cm^2 s^{-1}. This conclusion was further confirmed by the galvanostatic intermittent titration technique (GITT), as shown in Fig. 3f. According to the following equation:[39]

$$D = \frac{4}{\pi}\left(\frac{IV_m}{FS}\right)^2\left(\frac{dE/dx}{dE/dt^{1/2}}\right)^2 \quad (4)$$

where S is the surface area of the electrode. We calculated that the diffusion coefficient of Cu^{2+} ranges from 10^{-10} to 10^{-7} cm^2 s^{-1}, which is in good agreement with the EIS results. The rapid diffusion of Cu^{2+} lays the foundation for the excellent copper-ion storage capability of FeHCF.

To further understand the storage mechanism of Cu^{2+} in FeHCF, *in situ* XRD, Raman, and XPS were used to analyze the state changes of the FeHCF electrode during charge–discharge cycles. Fig. 4a–e and S9† show the *in situ* XRD results for the Cu-FeHCF battery. From the full spectrum in Fig. S9,† it is clear that in the initial state, the FeHCF electrode exhibits a diffraction pattern consistent with that of the FeHCF powder described earlier, where the diffraction peaks at 43.2° and

50.4° correspond to the window tape used in the testing cell. To better observe the impact of Cu^{2+} insertion and extraction on the FeHCF structure, typical diffraction peaks of crystal planes from the earlier cycles (Fig. 4a) were selected for further analysis, as shown in Fig. 4b–e. During the first discharge process, when Cu^{2+} ions are initially inserted, no significant change in the characteristic peaks of FeHCF is observed. However, as Cu^{2+} ions are nearly fully inserted, the diffraction peaks corresponding to (200), (220), and (400) disappear, and a new peak appears at 28.5°. During the first charge (Cu^{2+} extraction), the 28.5° diffraction peak gradually disappears, and the originally disappeared (200), (220), and (400) diffraction peaks reappear, indicating the gradual recovery of the FeHCF structure. Notably, these diffraction peaks show a shift towards higher angles compared to the initial FeHCF electrode. This transition is attributed to the incomplete removal of the inserted Cu ions or their partial substitution for Fe ions, leading to a slight distortion of the FeHCF lattice structure. The emergence of a new high plateau in subsequent cycles may also be associated with changes in the FeHCF framework. This is likely the cause of the initial capacity decay. In subsequent cycles, the diffraction peaks of various crystal planes showed regular changes, indicating that the FeHCF lattice structure undergoes reversible changes during the insertion and extraction of Cu^{2+} ions.

The Raman spectroscopy characterization of the FeHCF electrode at different charge–discharge states is shown in Fig. 4f and g. The vibration peaks in the 2000–2200 cm^{-1} range are attributed to C≡N stretching vibrations affected by Fe^{2+}/Fe^{3+}. In the initial state, two vibration peaks appear at 2096 cm^{-1} and 2153 cm^{-1}, which are consistent with those of the powder sample. After the first cycle, some residual copper ions caused a change in the relative intensity of the FeHCF vibration peaks, shifting them to higher wavenumbers at 2123 cm^{-1} and 2166 cm^{-1}. Upon further discharge, the extensive insertion of copper ions further affected the C≡N vibration, causing the peaks at 2123 cm^{-1} and 2166 cm^{-1} to shift to 2178 cm^{-1}, corresponding to the main peak. This change was reversed during the subsequent charging (Cu^{2+} extraction) process.

XPS shows the trend of elemental valence changes during the insertion and extraction of copper ions in FeHCF, as

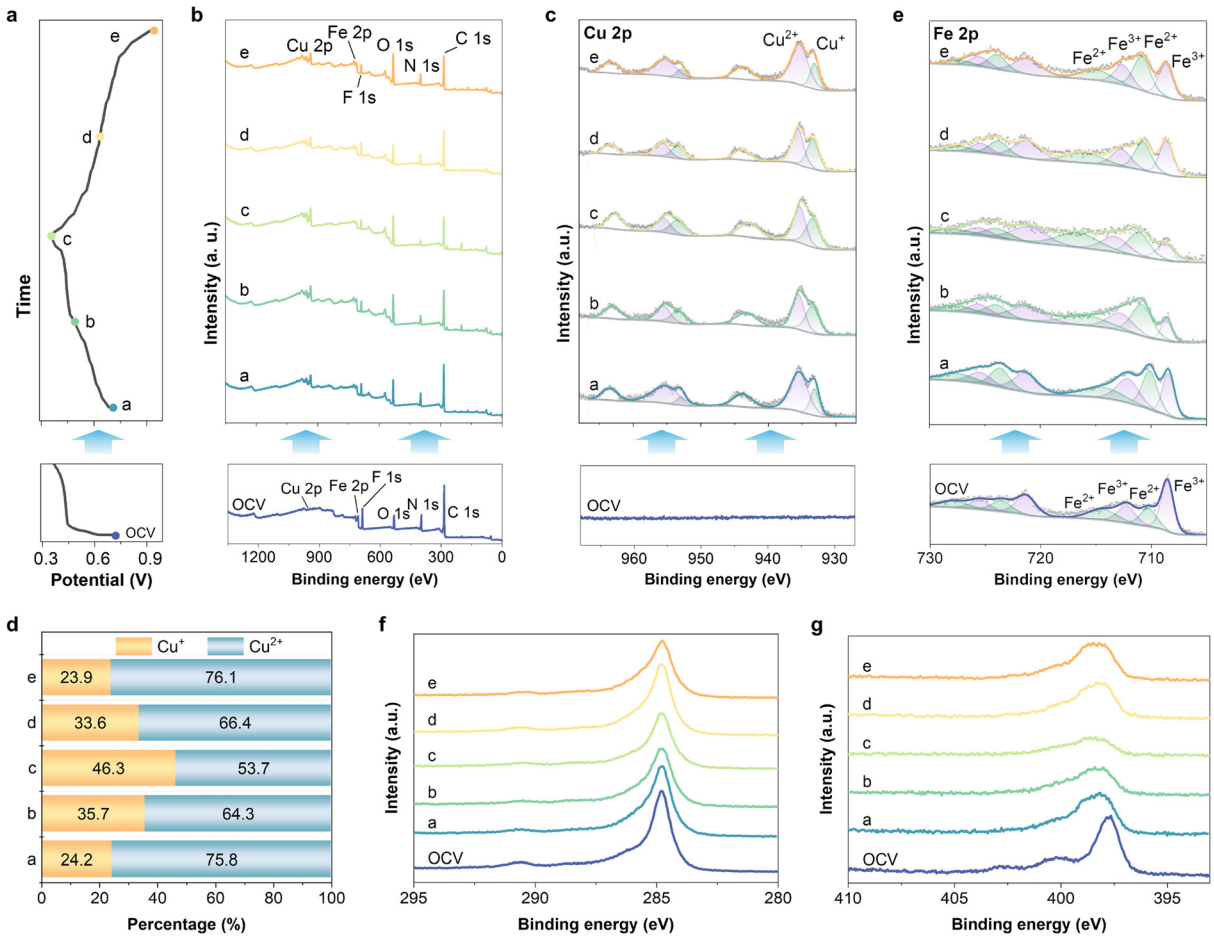

Fig. 5 (a) Charge and discharge curves. (b) XPS survey spectrum of the FeHCF electrode at the corresponding stages in panel (a). Core-level XPS spectra of (c) Cu 2p, (e) Fe 2p, (f) C 1s and (g) N 1s collected at the corresponding stages in panel (a), and (d) the change in the Cu^{+} and Cu^{2+} content ratio corresponding to the stage in (c).

shown in Fig. 5. In the initial FeHCF electrode, no Cu element was detected. After the first cycle, residual Cu was detected in the FeHCF electrode, indicating that not all inserted copper ions were extracted, which is consistent with the *in situ* XRD and Raman results.[40] At this point, the remaining copper ions include both Cu^{2+} and Cu^{+}, suggesting a partial conversion of Cu^{2+} to Cu^{+} during this process. In the subsequent discharge process, the intensity of the characteristic Cu 2p peaks gradually increases, as shown in Fig. 5a and b, indicating the insertion of copper ions. The detailed spectrum of the Cu 2p orbitals shows a change in the ratio of Cu^{2+} to Cu^{+} (Fig. 5c and d). Initially, Cu^{+} accounted for 24.2% of the total copper ion content, but as discharge progressed and Cu^{2+} was inserted, this value increased to 46.3%. This further confirms the conversion of Cu^{2+} to Cu^{+} during the process, as the insertion of only Cu^{2+} would not explain this change. The discharge process is the reverse of charging, with Cu^{+} being re-oxidized to Cu^{2+} and extracted, as indicated by the restoration of Cu^{+} content to 23.9%, accompanied by a decrease in the intensity of the Cu 2p characteristic peaks in the full spectrum. Corresponding changes are also observed in the Fe 2p spectrum (Fig. 5e). After the first cycle, the content of Fe^{3+} decreased, while that of Fe^{2+} increased, which correlates with the phenomenon of some copper ions remaining in the electrode. During subsequent copper ion insertion, more Fe^{3+} is reduced to Fe^{2+}, and the copper ion extraction process follows the reverse trend. The C 1s and N 1s characteristic peaks also exhibit systematic changes during the same cycling process, as shown in Fig. 5f and g.

While FeHCF demonstrates excellent copper-ion storage capability, using Cu as the anode results in a battery voltage of only around 0.25 V, limiting its practical applications. To increase the battery's operating voltage, it is essential to select an anode with a working potential much lower than the Cu^{2+}/Cu^{0} potential. Previous studies have shown that the Zn metal anode, in alkaline electrolytes, undergoes a $Zn/Zn(OH)_4^{2-}$ redox reaction, with a potential as low as −1.22 V *vs.* SHE.[41] At the same time, Zn metal electrodes offer a high theoretical capacity and a lower cost, making Zn an ideal candidate for increasing the battery's operating voltage.[42–44] By designing a decoupled battery system, the overall operating voltage can be effectively enhanced. The reaction process can be expressed as follows:

$$\text{Cathode}: \ \text{FeHCF} + x\text{Cu}^{2+} + 2x\text{e}^{-} \leftrightarrow \ \text{Cu}_x\text{FeHCF} \qquad (5)$$

$$\text{Anode}: \ \text{Zn} + 4\text{OH}^{-} \leftrightarrow \ \text{Zn(OH)}_4^{2-} + 2\text{e}^{-} \qquad (6)$$

The battery structure is shown in Fig. 6a, where the anode is a Zn metal electrode, and the cathode is the FeHCF electrode, with the anode side (alkaline electrolyte) and cathode side (acidic electrolyte) consisting of 1 M NaOH and 1 M $CuSO_4$, respectively. The middle section uses 1 M Na_2SO_4 as a

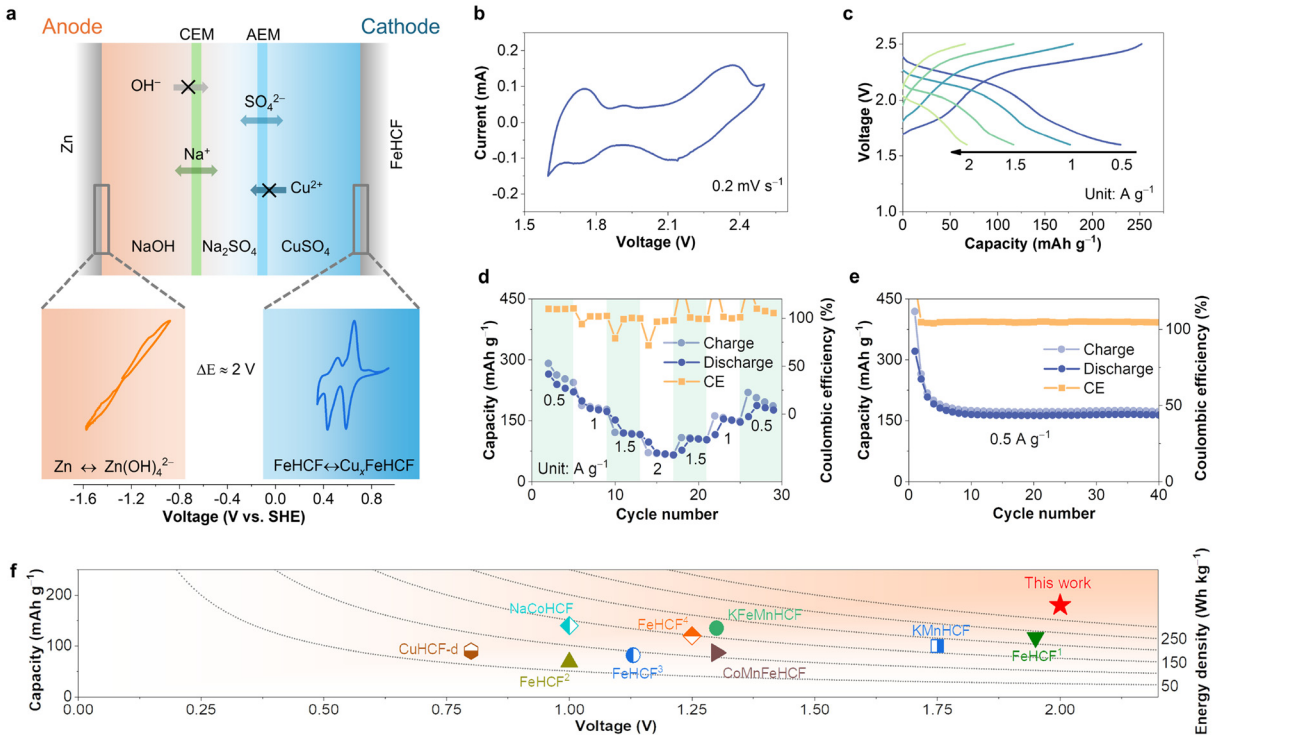

Fig. 6 Performance of the Zn//FeHCF decoupled battery. (a) Structure and mechanism diagram of the Zn//FeHCF decoupled battery. (b) CV curves recorded at 0.2 mV s^{-1}. (c) GCD curves at different current densities. (d) Rate performance of the Zn//FeHCF decoupled battery. (e) Electrochemical cycling stability at a fixed rate of 0.5 A g^{-1}. (f) Comparison of the Zn//FeHCF decoupled battery with recently reported batteries using PBAs as cathode materials.

salt bridge to balance the charge, and cation exchange membranes (CEMs) and anion exchange membranes (AEMs) separate the different electrolytes. The CV results of the Zn//FeHCF decoupled battery are shown in Fig. 6b, where two sets of redox peaks confirm its redox activity within the 1.6 V–2.5 V voltage range. Correspondingly, the GCD curves at different current densities also exhibit discharge plateaus at the corresponding potentials, as shown in Fig. 6c, with an average discharge voltage of around 2 V. As the current density increases, the voltage polarization difference gradually increases, which is due to the combined effect of ion transport in both the electrode material and the ion exchange membranes. As shown in Fig. 6d and e, at current densities of 0.5, 1, 1.5, and 2 A g^{-1}, the Zn//FeHCF decoupled battery exhibits capacities of 239, 180, 120 and 70 mA h g^{-1}, respectively. In conclusion, the constructed Zn//FeHCF decoupled battery demonstrates excellent storage capacity and operating voltage, which is undoubtedly advantageous compared to other recently reported aqueous batteries using PBAs as cathode materials, as shown in Fig. 6f.[18,23,34,45–50]

3. Conclusions

In conclusion, we have developed an aqueous copper-ion storage device based on FeHCF nanocrystal cathodes. FeHCF proves to be an efficient copper-ion storage material, delivering a high capacity of 190 mA h g^{-1} within a narrow voltage range of 0.6 V, with a stable discharge plateau at 0.59 V *vs.* SHE and a minimal polarization voltage of 0.2 V. The FeHCF cathode shows excellent rate performance, maintaining a substantial capacity of 102 mA h g^{-1} even at high current densities, attributed to the fast copper-ion transport. To further enhance the operating voltage, the Cu^{2+}/Cu^{0} anode reaction was replaced with the lower potential $Zn/Zn(OH)_4^{2-}$ reaction. This modification successfully extended the working voltage of the FeHCF-based battery, which operates within a voltage range of 1.6–2.5 V. These findings highlight the potential of FeHCF-based aqueous batteries for high-performance and safe energy storage applications.

Author contributions

Jinshu Zhang: writing – review & editing, writing – original draft, investigation, formal analysis, and data curation. Lexian Liu: investigation, formal analysis, and data curation. Yuao Wang: investigation and formal analysis. Yantuo Li: methodology and data curation. Yang Yang: data curation. Mingyi Ning: data curation. Jianxue Wu: data curation. Bingjie Ma: data curation. Wei Liu: writing – review & editing, supervision, investigation, and conceptualization.

Data availability

The data have been included in the paper or the ESI.†

Conflicts of interest

The authors declare that they have no known competing financial interests or personal relationships that could have appeared to influence the work reported in this paper.

Acknowledgements

The authors acknowledge the financial support from the National Key Research and Development Program of China (2022YFB3807200), the National Natural Science Foundations of China (22371041), the Open Fund of Key Laboratory for Intelligent Nano Materials and Devices of the Ministry of Education NJ2023002 (INMD-2023M08) and the SEU Innovation Capability Enhancement Plan for Doctoral Students (CXJH_SEU 24136). The authors thank the Center for Fundamental and Interdisciplinary Sciences of Southeast University for the support of *in situ* XRD and Raman measurements.

References

1 M. A. Giovanniello, A. N. Cybulsky, T. Schittekatte and D. S. Mallapragada, *Nat. Energy*, 2024, **9**, 197–207.
2 R. Fan, C. Liu, Z. Li, H. Huang, J. Feng, Z. Li and Z. Zou, *Nat. Sustain.*, 2024, **7**, 158–167.
3 J. Janek and W. G. Zeier, *Nat. Energy*, 2023, **8**, 230–240.
4 H. Wan, J. Xu and C. Wang, *Nat. Rev. Chem.*, 2024, **8**, 30–44.
5 J. Duan, X. Tang, H. Dai, Y. Yang, W. Wu, X. Wei and Y. Huang, *Electrochem. Energy Rev.*, 2020, **3**, 1–42.
6 G. Liang, F. Mo, X. Ji and C. Zhi, *Nat. Rev. Mater.*, 2021, **6**, 109–123.
7 L. Chang, J. Li, Q. Sun, X. Liu, X. Lu and H. Cheng, *Small*, 2024, 2408124.
8 D. Chao, W. Zhou, F. Xie, C. Ye, H. Li, M. Jaroniec and S.-Z. Qiao, *Sci. Adv.*, 2020, **6**, eaba4098.
9 M. Xia, J. Zhou and B. Lu, *Adv. Energy Mater.*, 2024, 2404032.
10 Y. Wang, T. Wang, P. Cui, G. Mao, K. Ye, F. Hu, M. Chen, D. Cao and K. Zhu, *Adv. Funct. Mater.*, 2025, 2421363.
11 H. Wu, J. Hao, Y. Jiang, Y. Jiao, J. Liu, X. Xu, K. Davey, C. Wang and S.-Z. Qiao, *Nat. Commun.*, 2024, **15**, 575.
12 K. Du, Y. Liu, Y. Zhao, H. Li, H. Liu, C. Sun, M. Han, T. Ma and Y. Hu, *Adv. Mater.*, 2024, **36**, 2404172.
13 T.-U. Wi, C. Park, S. Ko, T. Kim, A. Choi, V. Muralidharan, M. Choi and H.-W. Lee, *Nano Lett.*, 2024, **24**, 7783–7791.
14 V. D. Neff, *J. Electrochem. Soc.*, 1978, **125**, 886.
15 B. Singh, Y. Arya, G. K. Lahiri and A. Indra, *Coord. Chem. Rev.*, 2025, **523**, 216288.
16 C. Xu, Z. Yang, X. Zhang, M. Xia, H. Yan, J. Li, H. Yu, L. Zhang and J. Shu, *Nano-Micro Lett.*, 2021, **13**, 166.

17 X. Zhang, J. Zhang, H. Yu, T. L. Madanu, M. Xia, P. Xing, A. Vlad, J. Shu and B.-L. Su, *Angew. Chem., Int. Ed.*, 2024, e202414479.
18 L. Ma, S. Chen, C. Long, X. Li, Y. Zhao, Z. Liu, Z. Huang, B. Dong, J. A. Zapien and C. Zhi, *Adv. Energy Mater.*, 2019, **9**, 1902446.
19 W. Chang, J. Peng, W. Mao, Q. Wang, Y. Zhu and N. Peng, *Chem. Eng. J.*, 2024, **500**, 157204.
20 L. Wang, N. Liu, Q. Li, X. Wang, J. Liu, Y. Xu, Z. Luo, N. Zhang and F. Li, *Angew. Chem., Int. Ed.*, 2024, e202416392.
21 X. Bai, L. Zhang, D. Zhang, K. Li, T. Li, Y. Ren, H. He, B. Xie, G. Sun, J. Xu and X. Yin, *Chem. Eng. J.*, 2024, **497**, 154902.
22 J. Guo, F. Feng, S. Zhao, Z. Shi, R. Wang, M. Yang, F. Chen, S. Chen, Z.-F. Ma and T. Liu, *Carbon Energy*, 2023, **5**, e314.
23 Q. Yang, F. Mo, Z. Liu, L. Ma, X. Li, D. Fang, S. Chen, S. Zhang and C. Zhi, *Adv. Mater.*, 2019, **31**, 1901521.
24 Z. Liu, G. Pulletikurthi and F. Endres, *ACS Appl. Mater. Interfaces*, 2016, **8**, 12158–12164.
25 X. Wu, A. Markir, L. Ma, Y. Xu, H. Jiang, D. P. Leonard, W. Shin, T. Wu, J. Lu and X. Ji, *Angew. Chem., Int. Ed.*, 2019, **58**, 12640–12645.
26 H. Sun, M. Li, J. Zhu, J. Ni and L. Li, *ACS Nano*, 2024, **18**, 21472–21479.
27 C. Dai, L. Hu, H. Chen, X. Jin, Y. Han, Y. Wang, X. Li, X. Zhang, L. Song, M. Xu, H. Cheng, Y. Zhao, Z. Zhang, F. Liu and L. Qu, *Nat. Commun.*, 2022, **13**, 1863.
28 J. Lin, R. Chenna Krishna Reddy, C. Zeng, X. Lin, A. Zeb and C.-Y. Su, *Coord. Chem. Rev.*, 2021, **446**, 214118.
29 P. K. Pathak, K. P. Agrim, C. Park, H. Ahn and R. R. Salunkhe, *ACS Appl. Energy Mater.*, 2024, **7**, 11352–11360.
30 L.-P. Wang, P.-F. Wang, T.-S. Wang, Y.-X. Yin, Y.-G. Guo and C.-R. Wang, *J. Power Sources*, 2017, **355**, 18–22.
31 D. Du, Z. Zhu, K.-Y. Chan, F. Li and J. Chen, *Chem. Soc. Rev.*, 2022, **51**, 1846–1860.
32 S. Kumar, T. Salim, V. Verma, W. Manalastas and M. Srinivasan, *Chem. Eng. J.*, 2022, **435**, 134742.
33 M. Wang, H. Wang, H. Zhang and X. Li, *J. Energy Chem.*, 2020, **48**, 14–20.
34 L. Jiang, Y. Lu, C. Zhao, L. Liu, J. Zhang, Q. Zhang, X. Shen, J. Zhao, X. Yu, H. Li, X. Huang, L. Chen and Y.-S. Hu, *Nat. Energy*, 2019, **4**, 495–503.
35 W. Shu, J. Li, G. Zhang, J. Meng, X. Wang and L. Mai, *Nano-Micro Lett.*, 2024, **16**, 128.
36 T. Shang, J. Zhang, Y. Li, Y. Yang, J. Wu, M. Ning and W. Liu, *Batteries Supercaps*, 2024, **7**, e202300613.
37 Y. Wang, B. Wang, J. Zhang, D. Chao, J. Ni and L. Li, *Carbon Energy*, 2023, **5**, e261.
38 J. Zhang, Y. Wang, M. Yu, J. Ni and L. Li, *ACS Energy Lett.*, 2022, **7**, 1835–1841.
39 Y. Zhu, Y. Xu, Y. Liu, C. Luo and C. Wang, *Nanoscale*, 2013, **5**, 780–787.
40 Z. Zhang, Y. Li, G. Zhao, L. Zhu, Y. Sun, F. Besenbacher and M. Yu, *ACS Appl. Mater. Interfaces*, 2021, **13**, 40451–40459.
41 X. Zhang, B. Zhang, J.-L. Yang, J. Wu, H. Jiang, F. Du and H. J. Fan, *Adv. Mater.*, 2024, **36**, 2307298.
42 Y. Huang, Y. Wang, X. Peng, T. Lin, X. Huang, N. S. Alghamdi, M. Rana, P. Chen, C. Zhang, A. K. Whittaker, L. Wang and B. Luo, *Mater. Futures*, 2024, **3**, 035102.
43 C. Fan, W. Meng and J. Ye, *J. Energy Chem.*, 2024, **93**, 79–110.
44 Y. Wang, T. Wang, Y. Mao, Z. Li, H. Yu, M. Su, K. Ye, D. Cao and K. Zhu, *Adv. Energy Mater.*, 2024, **14**, 2400353.
45 Z.-L. Xie, Y. Zhu, J.-Y. Du, D.-Y. Yang, N. Zhang, Q.-Q. Sun, G. Huang and X.-B. Zhang, *Angew. Chem., Int. Ed.*, 2024, **63**, e202400916.
46 X. Wu, Y. Xu, H. Jiang, Z. Wei, J. J. Hong, A. S. Hernandez, F. Du and X. Ji, *ACS Appl. Energy Mater.*, 2018, **1**, 3077–3083.
47 X. Wu, J. J. Hong, W. Shin, L. Ma, T. Liu, X. Bi, Y. Yuan, Y. Qi, T. W. Surta, W. Huang, J. Neuefeind, T. Wu, P. A. Greaney, J. Lu and X. Ji, *Nat. Energy*, 2019, **4**, 123–130.
48 W. Deng, Z. Li, Y. Ye, Z. Zhou, Y. Li, M. Zhang, X. Yuan, J. Hu, W. Zhao, Z. Huang, C. Li, H. Chen, J. Zheng and R. Li, *Adv. Energy Mater.*, 2021, **11**, 2003639.
49 Z. Wang, Y. Xu, J. Peng, M. Ou, P. Wei, C. Fang, Q. Li, J. Huang, J. Han and Y. Huang, *Small*, 2021, **17**, 2101650.
50 Y. Zeng, X. F. Lu, S. L. Zhang, D. Luan, S. Li and X. W. Lou, *Angew. Chem., Int. Ed.*, 2021, **60**, 22189–22194.